Globular clusters with *Gaia*

E. Pancino,[1,2]★ M. Bellazzini,[3] G. Giuffrida[4,2] and S. Marinoni[4,2]

[1]*INAF-Osservatorio Astrofisico di Arcetri, Largo Enrico Fermi 5, I-50125 Firenze, Italy*
[2]*ASI Science Data Center, Via del Politecnico SNC, I-00133 Rome, Italy*
[3]*INAF-Osservatorio Astronomico di Bologna, Via Ranzani 1, I-40127 Bologna, Italy*
[4]*INAF-Osservatorio Astronomico di Roma, Via di Frascati 33, I-00044 Monteporzio Catone, Italy*

ABSTRACT

The treatment of crowded fields in *Gaia* data will only be a reality in a few years from now. In particular, for globular clusters, only the end-of-mission data (public in 2022–2023) will have the necessary full crowding treatment and will reach sufficient quality for the faintest stars. As a consequence, the work on the deblending and decontamination pipelines is still ongoing. We describe the present status of the pipelines for different *Gaia* instruments, and we model the end-of-mission crowding errors on the basis of available information. We then apply the nominal post-launch *Gaia* performances, appropriately worsened by the estimated crowding errors, to a set of 18 simulated globular clusters with different concentration, distance and field contamination. We conclude that there will be 10^3–10^4 stars with astrometric performances virtually untouched by crowding (contaminated by <1 mmag) in the majority of clusters. The most limiting factor will be field crowding, not cluster crowding: the most contaminated clusters will only contain 10–100 clean stars. We also conclude that (i) the systemic proper motions and parallaxes will be determined to 1 per cent or better up to $\simeq$15 kpc, and the nearby clusters will have radial velocities to a few km s^{-1}; (ii) internal kinematics will be of unprecedented quality, cluster masses will be determined to $\simeq$10 per cent up to 15 kpc and beyond, and it will be possible to identify differences of a few km s^{-1} or less in the kinematics (if any) of cluster sub-populations up to 10 kpc and beyond; (iii) the brightest stars ($V \simeq 17$ mag) will have space-quality, wide-field photometry (mmag errors), and all *Gaia* photometry will have 1–3 per cent errors on the absolute photometric calibration.

Key words: astrometry – parallaxes – globular clusters: general.

1 INTRODUCTION

The ESA[1] (European Space Agency) space mission *Gaia*[2] (Perryman et al. 2001; Mignard 2005; Gaia Collaboration 2016a,b) is the successor of *Hipparcos* (Perryman et al. 1997), with the goal of providing astrometry for billions of point-like sources across the whole sky, with an error of 24 µas-level for stars of $G \simeq 15$ mag. *Gaia* will also provide broad-band magnitudes and colours for all sources, down to the *Gaia* white-light magnitude of $G = 20.7$ mag ($V \simeq 21$ mag). Low-dispersion spectra will also be obtained in two broad-bands with the red and blue spectrophotometers (BP and RP). Finally, *Gaia* will produce spectra in the calcium triplet region with the RVS (the radial velocity spectrometer) down to $G \simeq 17$ mag, from which radial velocities (RVs). Object classifica-

tion and parametrization will be possible for all sources. *Gaia* was launched in 2013 December (de Bruijne, Rygl & Antoja 2014), and the first data release was in 2016 September (Gaia Collaboration 2016b), containing positions and white-light magnitudes for the best behaved stars, and additional information like parallaxes and proper motions for $\simeq$2 million stars observed previously with *Tycho-2* (Høg et al. 2000; Michalik, Lindegren & Hobbs 2015; Lindegren et al. 2016).

Gaia will observe not only stars, but also tens of thousands of quasars, unresolved galaxies, Solar system objects, many transient and variable objects like supernovae, and finally the interstellar medium (Altavilla et al. 2012; Ducourant et al. 2014; Eyer et al. 2014; de Bruijne et al. 2015; Proft & Wambsganss 2015; Zwitter & Kos 2015; Bachchan, Hobbs & Lindegren 2016; Tanga et al. 2016). *Gaia* will also pose a challenge because of its data amount and complexity, pushing the astrophysical community farther into the path of big data and data mining (Gaia Collaboration 2016a).

Gaia is limited in dense stellar fields, owing to the onboard and downstream telemetry bandwidth. For spectroscopy, an additional

limitation is provided by the large physical size of the dispersed images and spectra on the focal plane. This has particular relevance for studies of the Galactic plane, the bulge and globular clusters (hereafter, GCs). In the first few *Gaia* data releases, disturbed sources like binaries, multiple stars and stars in crowded fields will likely not be part of the released material (Gaia Collaboration 2016b). In any case, the inclusion of a sufficient sample of stars at the main-sequence turn-off point or fainter – with good-quality measurements – is very important for GC research. Therefore, only the latest few *Gaia* releases (2020–2023) are expected to provide a significant breakthrough in GC research. To prepare the work, we explore in this paper the expected behaviour of *Gaia* data in several simulated Galactic GCs, adopting the official post-launch *Gaia* science performances and some simplified recipes to describe additional deblending error components, based on the *Gaia* deblending pipelines. A very preliminary – and now outdated – version of this work was presented by Pancino, Bellazzini & Marinoni (2013).

This paper is organized as follows. In Section 2, we describe the current status of crowding treatment in *Gaia*; in Section 3, we present our crowding errors modelling; in Section 4, we describe our simulated clusters and the computation of *Gaia* observed quantities and final errors; in Section 5, we explore the simulations and show the potential of *Gaia* data for GC studies; in Section 6, we summarize the main results and draw our conclusions.

2 CROWDING IN *GAIA* DATA

As mentioned in the previous section, *Gaia* is a complex space mission, with two different telescopes projecting their light on a large common focal plane, captured by 106 different CCDs (charge-coupled devices), and passing through different instruments. *Gaia* scans the whole sky by precessing its spin axis, and describing great circles on the sky that slowly drift with its precession. Each region is scanned from a minimum of ≃40 times, to a maximum of ≃250 times, with an average number of ≃70 passages for the AF, BP and RP, and ≃40 passages for RVS. All the CCDs in the focal plane are read in TDI (time-delayed integration) mode to closely follow *Gaia*'s movement across the sky. On the focal plane, stars 'move' along the scanning direction, encountering different instruments:

(i) The first two columns of the CCD array are called Sky Mappers (SM), and they are used for the onboard detection of point-like sources; each of the SM columns sees only light from one of the two telescopes.

(ii) The AF (astrometric field) provides astrometry and photometry of point-like sources in the *G* band, a white-light passband defined by the telescope and instrument transmission and by the CCD quantum efficiency (Fig. 1).

(iii) The BP and RP provide low-resolution spectra ($R = \lambda/\delta\lambda =$ 20–100) in the ranges shown in Fig. 1, and the integrated G_{BP} and G_{RP} magnitudes; the spectra are necessary for the chromaticity displacement correction in astrometric measurements.

(iv) The RVS provides $R \simeq 11\,700$ spectra in the calcium triplet region, for stars down to $G \simeq 17$ mag, depending on the object.

To save telemetry bandwidth, given the enormous amount of data produced daily by *Gaia*, observations in each instrument are only transmitted for pixels contained in rectangular windows, that follow the detected point-like objects along the focal plane. For the faint stars, data in the allocated windows are binned in the AC direction by the onboard processing software. The adopted window sizes and relevant quantities for our treatment of crowding are listed in
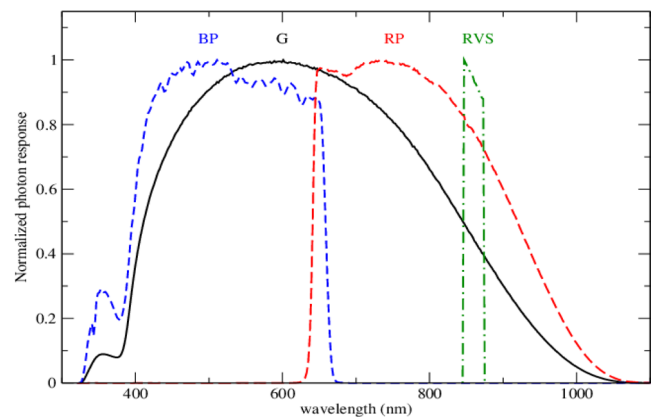
Figure 1. The *Gaia* nominal passbands for the astrometric field (*G* band), the blue and red spectrophotometers (BP and RP) and the radial velocity spectrometer (RVS). Figure courtesy of C. Jordi.

Table 1. Adopted *Gaia* relevant quantities. We note that the AF window sizes are relevant for the astrometry; the BP/RP sizes for the photometry, chromaticity correction, and object classification and parametrization; the RVS window sizes are relevant for RV, object parametrization and abundance analysis.

Size (arcsec)	Size (pix)	Description
0.176 789	1 (AC)	Across scan (AC) pixel size
0.058 933	1 (AL)	Along scan (AL) pixel size
0.176 789	3 (AL)	*Gaia* PSF
2.121 468	12 (AC)	AC window size (AF, BP and RP)
0.070 720	12 (AL)	AL window size (AF)[a]
1.767 890	10 (AC)	AC window size (RVS)
3.535 980	60 (AL)	AL window size (BP and RP)
74.785 977	1269 (AL)	AL window size (RVS)

[a]In some CCD columns in AF, as well as in the SM CCD columns, the windows are longer to allow for background measurements around the sources. The longer wings of these windows can in principle be used also to check the source profile behaviour outside normal window limits.

Table 1. More information can be found in the *Gaia* mission paper (Gaia Collaboration 2016a).

2.1 *Gaia* deblending and decontamination pipelines

Crowding treatment ideally requires a preliminary evaluation of the crowding conditions of each source and transit, based on knowledge of the *scene*, i.e. the distribution and characteristics of all the neighbouring sources, as collected before the current observation. Different pipelines are employed for different instruments and to treat different cases. Below we describe the current status of the ones that are relevant for this study.

2.1.1 AF deblending

Stars closer than the *Gaia* PSF width (which is assumed here[3] to be 0.177 arcsec, see also Table 1) can be recognized as blends already in the astrometric processing of AF data. These blends can be detected, for example, from the high errors in the centroid

---

[3] The value we adopted is a conservative estimate. The *Gaia effective* PSF varies across the field of view and has a median value of 0.103 arcsec (Fabricius et al. 2016).
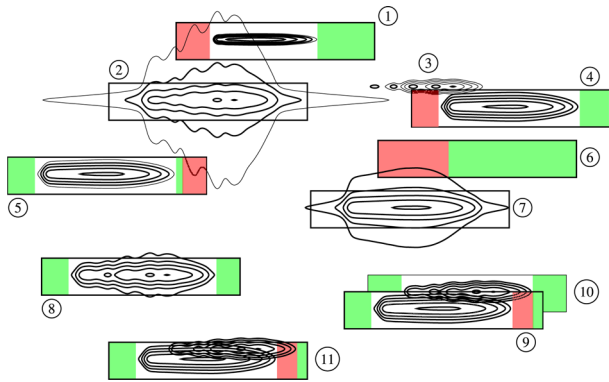
Figure 2. An illustration of the crowding effects on BP and RP dispersed images, with their assigned windows (black rectangles). Different cases are represented, some going beyond the scope of this paper. Stars are represented by their surface density profiles (solid contours), with the outmost contours at the background level. The brightest star ($G = 15$ mag) is in window (2), while the faintest one ($G = 20$ mag) is in window (1). Stars fainter than the *Gaia* magnitude limit ($G = 20.7$ mag) are assigned no window, like for star (3). The coloured portions of the windows are the background samples, in green when they are free from contamination, and in red when they are contaminated and cannot be used. When stars are too close, they can be assigned to the same widow or two (or more) truncated windows, like in cases (9), (10) and (11). There are also empty windows (virtual objects) like in case (6). Figure courtesy of A. Brown.

determination and its wobbling from one transit to another, or by photometric variability, RV variability, or in general because the fits of the PSF or LSF to the data show large residuals or require more than one component.

Assessing whether a star is isolated or has detected or suspected companions is a crucial task. Multiple or blended objects are redirected to the NSS (non-single stars) pipeline where an attempt to model them as binary systems is carried out (Pourbaix 2011; Gaia Collaboration 2016a). If none of the available binary models or configurations produces a good fit to the data, then a stochastic model is employed to derive preliminary parameters of the secondary (or tertiary and so on) source. Therefore we can assume that – considering also the small *Gaia* PSF – the vast majority of NSS will be known.

Stars that are further apart than the tiny *Gaia* PSF are easily deblended by the PSF fitting algorithms, with results much more similar to *HST* (*Hubble Space Telescope*) than to typical ground-based telescopes. This is the main reason why – as we will see in the following – astrometric measurement uncertainties (and G magnitudes) are in general less affected by crowding, unlike BP/RP and RVS measurements.

2.1.2 *BP and RP deblending and decontamination pipelines*

BP and RP transits of sources that are not isolated will be called here either *blended* or *contaminated*. The idea is that when the sources are so close that they occupy the same window or interfering windows in the vast majority of the transits (*blends*, with $D < 2.12$ arcsec), they will require a different treatment than objects that will often be assigned well-separated windows, or transits that are just altered by the flux of a bright source that is well outside of the window (*contaminants*, with $D < 3.54$ arcsec). This is illustrated in Fig. 2, where different cases are shown together with the background evaluation regions, and in Fig. 3, showing how the differing orientation and AL projected distance between sources affects window assignment.
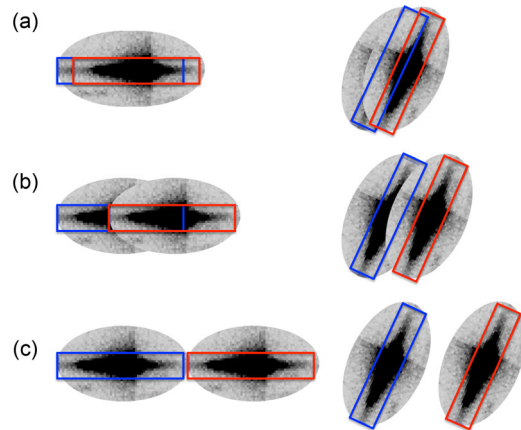
Figure 3. Simplified description of transits in BP/RP. In case (a), two stars are closer than half the AC window size, and no matter the orientation of the satellite, they will always be assigned the same window (or truncated windows). In case (b), two stars have a distance that is in between the AC and AL half window sizes, and depending on the orientation, they are sometimes assigned the same window (or truncated window), sometimes different windows. Depending on their brightness, they can still contaminate each other's window. In case (c), the stars are farther apart than the AL window size, and they are always assigned two different windows but, if one of the two stars is very bright, it can still contaminate the other significantly.

For blended sources, there are different pipelines that can be used in different phases of the mission. Blind pipelines (without knowledge of the scene) can be applied in the initial phases, when the history of each source in different instruments has not built up to a sufficient level. The two (or more) blended sources can be roughly modelled without a priori knowledge of their exact positions, astrophysical parameters and fluxes, just by modelling them with two overlapping spectral energy distributions. This approach was successfully applied to *Gaia* commissioning data[4] of bright stars, recovering the vast majority of the Ticho-2 binary and double stars. Once a few transits are accumulated, they can be better disentangled if they are modelled simultaneously (*per source* rather than *per transit*), even if there is still not enough information on the scene, improving the quality of the reconstruction. Finally, once the scene is well characterized and the history of the source is well developed, other parameters of the modelling like the spectral type, the projected distance of the sources along scan and the relative fluxes, can be used to further improve the involved sources reconstruction.

For contaminated sources, it is necessary to know well the flux of the contaminating sources around, thus knowledge of the scene is necessary. Each known source is modelled to reconstruct the flux even at large distances from the window (especially for bright stars). The amount of reconstructed contaminating flux from neighbouring sources is computed in each pixel of the contaminated source window, and subtracted. For all these reasons, decontamination will have to be performed contextually with the scene reconstruction and crowding evaluation.

2.1.3 *RVS deblending and decontamination pipelines*

The deblending philosophy adopted by RVS is slightly different from the one adopted in AF, or BP and RP. The deblending pipelines are being adapted and rewritten to mitigate the stray light issues

[4] http://www.cosmos.esa.int/web/gaia/iow_20150226

found after launch[5] (Mora et al. [2016]) that impact mostly on RVS spectra, with an expected loss of $\simeq 1.4$ mag in sensitivity (Seabroke et al. [2016]). We therefore based our modelling of deblending errors on a previous algorithm that was based on general geometrical considerations (Allende Prieto [2008]).

The treatment of contamination is instead part of the background treatment, which is a vital part of RVS processing, because of the length of the spectra (see Table [1]). The background is divided in diffused and point-like, and treated separately. In both cases, a modelling takes place based on knowledge of the scene and all available data on stray light and nearby objects. The model produces an estimate of the total background in the RVS windows that is subtracted from the source signal. Clearly, the model becomes more and more accurate as *Gaia* data are progressively accumulated and therefore the best results will be obtained towards the end of the mission (Janssen, Huckle & Seabroke, private communication).

2.1.4 Image reconstruction and future possibilities

To facilitate the study of crowded areas, two paths are being followed. On the one hand, some crowded regions like the centre of *ω* Centauri or NGC 1818 in the Magellanic Cloud were imaged and transmitted to the ground in 2D mode in the SM,[6] during commissioning, and further regions might be observed in 2D during the mission lifetime. The goal of these 2D images is to fully reconstruct the *scene* around each *Gaia* source to help improving and testing the deblending algorithms in crowded areas.

On the other hand, pipelines for the 2D image reconstruction from individual *Gaia* transits are being developed. One such pipeline, called Source Environment Analysis (sea) pipeline, is based on the FastStack image reconstruction (Harrison [2011]; Gaia Collaboration [2016a]). The initial tests are promising and the reconstructed images could be useful, among other things, to test and improve the deblending and decontamination pipelines as well.

Therefore, the simulations presented in this paper, being based on the current status of the deblending and decontamination pipelines, have to be seen as generally pessimistic.

2.2 A note about completeness in *Gaia* data

A particular limitation of the *Gaia* design is related to the number of simultaneous object and background (virtual object) windows that can be allocated by the onboard detection algorithm in each CCD and in any given moment. This number varies from $\simeq 35\,000$ to $1\,050\,000$ objects per square degree, depending on the instrument (see Gaia Collaboration [2016a], for more details). Areas of the sky that can suffer from this limitation are clearly the Galactic bulge and plane, and all other fields of view that happen to overlap them on the *Gaia* focal plane.[7] More relevant to this study, the limitation applies to the central regions of GCs, where the local star density can be very high.

At the single transit level, completeness is also influenced by the onboard detection algorithm. Every source that enters the SM is
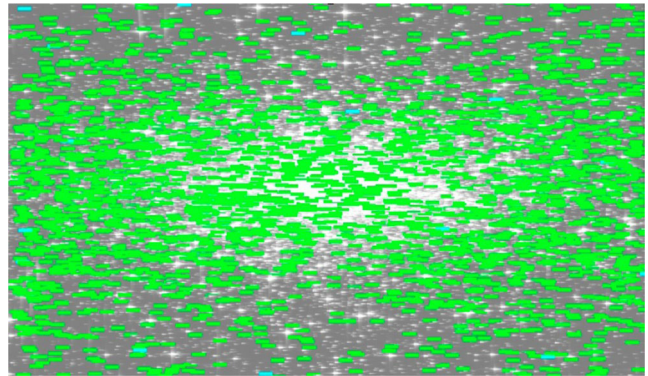
Figure 4. Effect of the onboard detection on completeness. The BP/RP image of a GC was simulated with GIBIS (Babusiaux [2005]). The green rectangles are the assigned windows. There is an apparent loss of stars above and below the cluster centre, where the AC stellar density is lower and windows have a lower probability of being assigned to a source. The percentage of stars lost is roughly constant with stellar density in each transit, but each transit has a different orientation. As a results, the end-of-mission incompleteness will tend to be flatter with distance from the centre than in usual GC photometries.

assigned a window, prioritizing brighter objects down to the limiting magnitude. The windows follow the stars along the focal plane as *Gaia* scans the sky, and when the stars exit the field, the window slots are 'freed' and can be assigned to new sources again. For this reason, the central dense areas of the clusters will – statistically speaking – contain more (bright) stars, and thus obtain more windows with respect to the periphery of the cluster, in the AC direction. Different scans, oriented in the sky with different angles, will lose different stars and thus at the end of mission, each star that is not entirely lost will have lost part of its transits. This is illustrated in the simulated cluster in Fig. [4], and is also visible in the *ω* Centauri actual *Gaia* data shown in a press release.[8]

We do not attempt to simulate these completeness effects in this paper, as they would require a full end-of-mission simulation of different lines of sight in the sky, including the detailed behaviour of the onboard detection algorithms.

3 MODELLING OF CROWDING ERRORS

As mentioned above, our goal is to illustrate what *Gaia* can do for GC studies, rather than attempting a rigorous simulation of deblending errors. Therefore, we will model available simulations of crowded *Gaia* data, to derive simple formulas with as few free parameters as possible.

The crowding error models derivation for different *Gaia* instruments and different types of blends are described in the following sections. The models describe the expected percentage errors on flux caused by crowding as a function of relevant parameters like the contaminating flux, contaminating colour, and distance of the contaminating object(s).

Later, in Section 4 we will transform our flux errors into errors on other parameters like positions, parallaxes, proper motions and RVs. We will then use these errors to worsen the nominal *Gaia* post-launch science performances, depending on the crowding level suffered from each of our simulated GC stars.

---

[5] http://www.cosmos.esa.int/web/gaia/news_20141217

[6] http://www.cosmos.esa.int/web/gaia/iow_20140206

[7] We recall that to obtain absolute astrometric measurements, *Gaia* projects two different lines of sight on a common focal plane. To disentangle sources coming from the two projected lines of sight, each of the SM CCD columns sees only one of the lines of sight. Therefore, there will be some fields that – even with low stellar background – will happen to overlap crowded areas in some fraction of their transits.

[8] http://www.cosmos.esa.int/web/gaia/iow_20141113

3.1 'Classic' blends

We term in this paper *classic blends* those stars that are closer than the AF *Gaia* PSF (0.177 arcsec, see Table 1), and that will remain so along the five years of *Gaia* observations. Stars that will move apart thanks to their parallax or proper motion differences, or that have RV differences that allow to deblend them, will not be considered as classic blends, but treated as normal *Gaia* blends (see below).

The precession of *Gaia* has an important implication for crowding treatment: each time *Gaia* scans a particular region of the sky, it is oriented differently, and thus the projected distance of two stars in the SM columns, on which the onboard object detection and window assignment are based, are different (see Fig. 3). Therefore, as described in Section 2.1.1, even the closest classic blends have a chance to be deblended, although it is difficult to simulate realistically the errors caused by deblending when so many observables enter iteratively the deblending procedure along the whole mission.

In this paper, we will assume that all blends of stars closer than the *Gaia* PSF will be recognized as such, thanks to the mission long lifetime, its tiny astrometric and photometric errors, and sophisticated data analysis methods. Because of the limited number of classic blends,[9] this assumption is not going to have a significant impact on the following analysis. If the relatively small number of classic blends comes as a surprise, it has to be noted that *Gaia* observations only reach $V \simeq 21$ mag in GCs, and thus the actual crowding levels are much lower than those of the typically deeper photometry from the ground or with *HST*.

We will also assume that the actual deblending errors follow the relation adopted for the BP and RP blends (see below), extrapolating the present simulations towards smaller source distances. While highly uncertain, this is our only available estimate of the *Gaia* deblending capabilities at the present stage. For RVS, there currently are no plans to attempt deblending of sources closer than 0.17 arcsec, and therefore we will not attempt to simulate the effect of crowding in these RVS sources.

3.2 'Gaia' blends

As discussed in Section 2.1.2, *Gaia* blends are all those cases in which two stars are closer than half the AC window size of the relevant instrument (Table 1, these all fall into case (a) of Fig. 3). Because the AF image deblending will be simpler (the AL profile is sharper) than that of BP, RP and RVS spectra, we will conservatively base our estimate of crowding errors for deblending on a set of BP and RVS simulations.

For the BP and RP blending simulations, we used a per-transit, partially informed deblending pipeline[10] on the GIBIS (Gaia Instrument and Basic Image Simulator; Babusiaux 2005) simulated BP spectra of a typical GC red giant, with $T_{eff} = 4000$ K and $G = 15$ mag. The star was blended with other similar stars, having either

---

[9] From 5 to 8 per cent of the total number of stars in our simulations, including field stars, are classic blends, depending on the particular cluster. The classic blends are mostly in the inner parts of GCs, within 1 arcmin approximately. For more details see Section 4.4.

[10] For a detailed description of the various BP/RP deblending pipelines, see Section 2.1.2. What we mean here by 'partially informed' is that we used information on the blended stars positions in AF, but we did not use any other information, such as astrophysical parameters (T_{eff}, $\log g$, A_V, [Fe/H]) and therefore we assumed we did not know the spectral energy distribution of the involved sources. This is still a pessimistic assumption, because towards the end of the mission this kind of information will become available and iteratively improved with every data processing cycle.
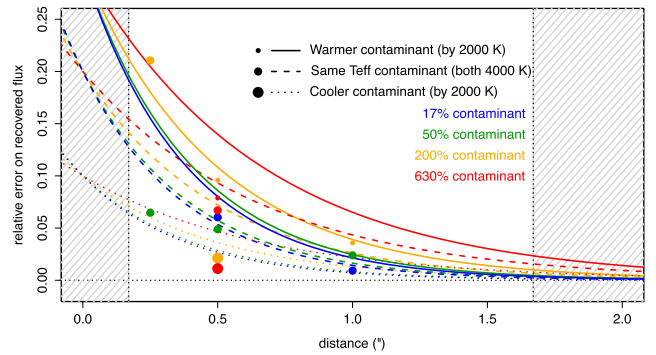
Figure 5. The simulated BP deblending errors as a function of distance (circles), based on a $G = 15$ mag star with $T_{eff} = 4000$ K, and our derived error models (curves). The dotted vertical lines mark the applicability range, from the *Gaia* PSF size (0.177 arcsec) to half the length of the BP/RP windows (1.76 arcsec). Blends with different characteristics are shown: cooler by 2000 K (small circles and solid curves), with the same temperature (medium circles and dashed curves), and hotter by 2000 K (large circles and dotted curves). The colours refer to the relative contaminating flux: 17 per cent (blue), 50 per cent (green), 200 per cent (yellow) and 630 per cent (red).
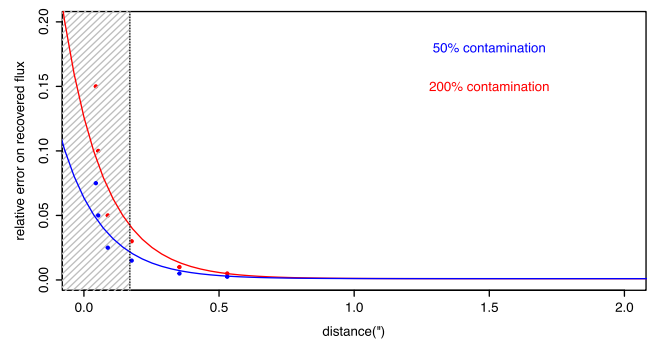
Figure 6. The simulated pre-launch RVS deblending errors, for different contamination levels, and our simplified exponential fits. The shaded area ($D < 0.17$ arcsec) is not yet treated in the current RVS deblending pipelines, and our fits there are extremely uncertain, therefore we will not provide any simulation for classic blends in RVS.

$T_{eff} = 4000$ or 6000 K, $G = 15.75$ or 17.00 mag, and at different distances equal to 0.25, 0.5 and 1.0 arcsec (see Fig. 5).

We then modelled the deblending (relative) errors on the recovered flux as an exponential $\alpha e^{\beta D}$, where D is the distance between the two blended stars. The coefficients α and β vary with the temperature difference and the relative contaminating flux, respectively, as illustrated in Fig. 5. For RP, the deblending errors were arbitrarily multiplied by 1.5, owing to the generally wider AL shape of the spectra that produces worse deblending results than in BP. These simplified recipes are intentionally pessimistic, to accommodate for unexpected sources of error. The approximate range of validity of the model (highlighted in Fig. 5) goes from the *Gaia* PSF size to half the AL size of the BP and RP windows. As discussed in the previous section, we applied an extrapolation of this relation to $D < 0.17$ arcsec to classic blends, for lack of a more detailed study at this stage.

For RVS, the only available deblending simulations were computed before launch (Allende Prieto 2008, see also Fig. 6), when the windowing scheme and background treatment were different (see Section 2.1.3). Thus, the error modelling presented here will be much more uncertain for RVS than for BP and RP, or for AF.

The temperature or colour difference between two sources has little impact on the deblending ability of the RVS pipelines, because the spectral shape is approximately flat along the RVS windows. What mostly counts is the relative contaminating flux. As a result, the best-fitting exponential laws had a constant β, and α varying with the relative contaminating flux. As mentioned above, we did not extend the model below the PSF size for RVS (shaded region in Fig. 6).

3.3 Contaminants

For contaminated stars [cases (b) and (c) in Fig. 3], the reconstruction of star fluxes at distances larger than the window size is subject to a variety of uncertainty sources, and the relevant pipelines will be effective only when a sufficient history is accumulated to build a scene. Not only the stars positions are needed, but also their spectral energy distributions. Additionally, a complete characterization of the PSF profiles AC and AL, at different wavelengths and positions on the focal plane will be fundamental. Therefore no detailed simulations are available at the moment (Section 2.1.2).

However, we do know that a step-like behaviour is expected in the errors at 1.76 arcsec, where the processing switches from decontamination to deblending, in the sense that decontamination pipelines perform slightly worse than the deblending ones. There will be, on purpose, a 'grey area' in projected distance between sources, where both pipelines will be applied, for cross-validation purposes. Some tests were performed to develop the current decontamination algorithms (Piersimoni, De Luise & Busso 2011, and De Luise, private communication). According to those tests, we decided to roughly approximate the decontamination errors with a factor of 2 worsening with respect to deblending errors. This is a pessimistic assumption.

Our modelling of decontamination residual errors is applied to contaminant stars with distances ranging from half the AC window size to the full AL window size or to the contaminating star's 'size', whichever is larger. We modelled the contaminating stars sizes as a linear function of G magnitude (Pulone & Marrese, private communication, see also Fig. 2). Stars fainter than $G \simeq 15$ mag are generally smaller than the BP and RP AL window size.[11]

For RVS, the discrete background pipelines are being presently integrated and tested, so no simulations are available at the moment and we just extended our simplified treatment of the RVS blends (previous section) to RVS contaminants, as done for BP and RP, using the appropriate window sizes.

4 CLUSTER SIMULATIONS

We simulated 18 different GCs, as summarized in Table 2, with different concentration, background contamination and distance. The final simulated clusters, after the *Gaia* science performances and the crowding error simulations are included, are presented in Table 3.

4.1 3D simulated clusters

The simulated clusters were computed with the MCLUSTER code[12] (Küpper et al. 2011), that is designed to produce initial conditions

---

[11] With our linear relation, a $G = 2$ mag star would be able to significantly contaminate stars up to 34.4 arcsec. These bright stars are rare: in our 18 simulated GCs there is only one field star brighter than that, appearing in the six disc GCs.

[12] https://ahwkuepper.wordpress.com/mcluster/
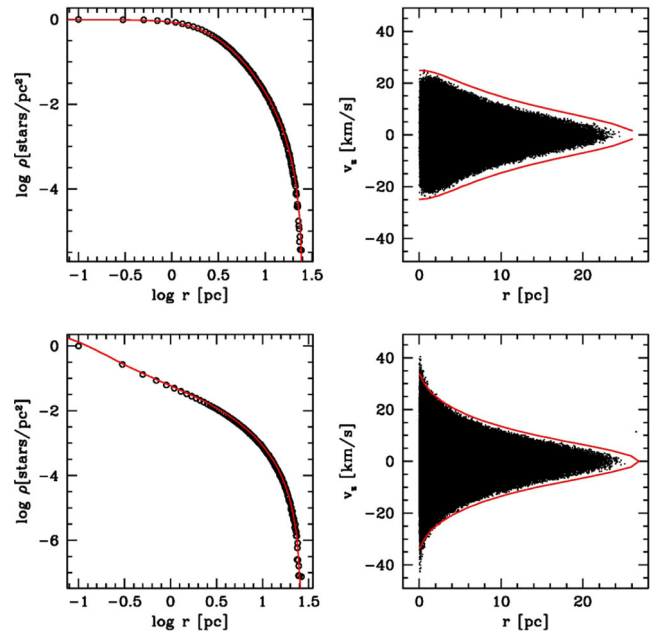
Figure 7. The logarithmic density profiles (left-hand panels) and RV dispersion profiles (right-hand panels) for the two synthetic clusters with concentration parameter $c = 1.0$ (top panels) and $c = 2.5$ (bottom panels). The red lines are the corresponding theoretical density profiles (left-hand panels) and $\pm 3\,\sigma$ contours about the systemic velocity for King (1966) models with the same parameters.

for *N*-body simulations. We used the code version (*mcluster_sse*) that implements the stellar evolution recipes by Hurley, Pols & Tout (2000).

We produced two clusters containing 800 000 stars, with positions and velocities drawn from equilibrium King (1966) models. The two clusters differed only in their concentration parameter, $c = \log(r_{\mathrm{t}}/r_{\mathrm{c}})$, one having $c = 1.0$ and the other $c = 2.5$ (see also Fig. 7). Among the key input parameters for the simulation, the half-mass radius was chosen to produce a (projected) half-light final radius similar to what typically observed for Galactic GCs: 4 pc for the $c = 1.0$ cluster and 3 pc for $c = 2.5$ one (see also Harris 1996, and following updates). Among the key input stellar population parameters, we adopted an age of 12 Gyr, a metallicity of $Z = 0.0003$, corresponding to [Fe/H] = -1.79 dex, and a Kroupa (2001) IMF (initial mass function). The simulations were performed without including binaries, for simplicity, and the resulting clusters are spherical and non-rotating.

The main implications of our choices of input parameters are: (i) a blue HB (horizontal branch) morphology, which may be useful to test the performance of *Gaia* on relatively hot stars and (ii) a stellar M/L_{V} ratio larger (≥ 3 instead of ≤ 2) than what typically observed in Galactic GCs having a present-day mass function compatible with a low-exponent power law (Paust et al. 2010). The high M/L_{V} ratio is also due to a relatively large fraction of dark remnants: $\simeq 25$ per cent of the cluster mass is contributed by objects with $M > \mathrm{M}_{\odot}$.[13] Independently of the recipes giving raise to such a large fraction of dark remnants and their actual nature, this is not a concern for our purpose: the only effect is that the potential well may

---

[13] Dark remnants are white dwarf stars, neutron stars and black holes. Recently, comparable fractions of dark remnants were obtained with state-of-the-art cluster modelling by Sollima et al. (2015, 2016).

Table 2. Simulated cluster properties and crowding evaluation results. For each of the 18 simulated GCs we list (see the text for more details): (1) the GC ID number; (2) the GC concentration parameter, $c = \log(r_{\mathrm{t}}/r_{\mathrm{c}})$; (3) the GC projected distance; (4) the type of simulated background; (5) the total number of simulated stars (GC and background) above *Gaia* detection limit; (6) the number of GC members; (7) the number of classic blends; (8) the number of *Gaia* blends; (9) the number of contaminated stars; (10) the number of clean stars, i.e. contaminated by less than 0.1 per cent in flux (roughly 1 mmag); (11) the quick GC designation used in the paper and (12) some examples of GCs with similar distance, concentration and background field contamination.

Cluster	c (dex)	Distance (kpc)	Background	n_{tot}	n_{GC}	n_{classic}	n_{blends}	n_{contam}	n_{clean}	Designation	Similar to
# 1	1.0	5	halo	73 385	72 510	4621	45 101	52 142	16 093	Easy case	M13, M92
# 2	1.0	10	halo	30 200	29 325	3521	21 550	23 754	4275		M92
# 3	1.0	15	halo	14 027	13 152	2203	10 312	11 203	1495		NGC 5053
# 4	1.0	5	disc	54 923	26 816	1028	14 115	17 289	7379		M71
# 5	1.0	10	disc	33 435	5328	326	3302	3812	1164	Intermediate case	M56, NGC 2298
# 6	1.0	15	disc	29 737	1630	123	1048	1208	311		M79
# 7	1.0	5	bulge	1537 592	71 996	9833	69 887	71 600	218		M22, NGC 6553
# 8	1.0	10	bulge	1494 601	29 005	5620	28 497	28 919	36		M9, NGC 6638
# 9	1.0	15	bulge	1478 538	12 942	2998	12 762	12 911	15		Pal 11
# 10	2.5	5	halo	73 385	72 510	11 902	47 043	53 029	15 623		M5
# 11	2.5	10	halo	30 200	29 325	6914	21 977	23 944	4117		M3
# 12	2.5	15	halo	14 027	13 152	3663	10 407	11 176	1525		NGC 5466
# 13	2.5	5	disc	54 923	26 816	3236	15 372	18 085	6946		M92, Pal 10
# 14	2.5	10	disc	33 435	5328	906	3491	3968	1055		M79, NGC 1851
# 15	2.5	15	disc	29 737	1630	292	1097	1250	300		M15
# 16	2.5	5	bulge	1537 592	71 996	16 564	70 125	71 648	190		NGC 6540, NGC 6558
# 17	2.5	10	bulge	1494 601	29 005	8726	28 556	28 924	40		NGC 6325, NGC 6342
# 18	2.5	15	bulge	1478 538	12 942	4378	12 770	12 914	13	Difficult case	M54, NGC 6517

be slightly deeper than for most real clusters and, consequently, the velocity dispersion is slightly larger, at fixed total luminosity and scale radius. What is relevant for us is that the central velocity dispersion is still in the right range and that the model is self-consistent.

The resulting simulated clusters have absolute integrated magnitudes of $M_{\mathrm{V}} = -7.6$ mag, i.e. just above the peak of the clusters luminosity function ($M_{\mathrm{V}} = -7.4$ mag, according to Brodie & Strader 2006). The clusters projected surface density distributions are well fitted by a King (1966) profile, when obtaining r_{c} (the core radius) from the fit. Finally, the derived central velocity dispersions agree well with the predictions by King (1966), where the total mass is obtained by summing the masses of all individual stars.

4.2 Simulated field contamination

We simulated the field Galactic population in three directions using the Besançon models[14] (Robin et al. 2003, and references therein), including kinematics and without observational errors. The models produced catalogues of magnitudes (in the Johnson–Cousins system), 3D positions, and 3D motions. We adopted the 'standard' extinction law offered by the Besançon simulator, a mean and diffused absorption of 0.7 mag kpc^{-1}, neglecting small-scale variations, and decreasing away from the Galactic plane with a smooth Einasto profile (for more details, see Robin et al. 2003). We selected all available spectral types in a magnitude range of $0 < V < 25$ mag. The simulations were computed in a 0.7×0.7 deg^2 centred on each of the following three directions (see also Table 2):

(i) a rather empty *'halo'* field at $l = 150$ and $b = 80$ deg, containing $\simeq 2300$ stars in total; this is meant to represent the best cases of low background contamination in *Gaia* observations;

(ii) an extremely dense *'bulge'* field at $l = 5$ and $b = 5$ deg, containing almost 6 millions of stars, which should cover even the most crowded *Gaia* observations, when two relatively crowded lines of sight overlap on the focal plane (see also Section 2);

(iii) a crowded *'disc'* field in the anticentre direction, at $l = 180$ and $b = 0$, containing roughly 140 000 stars, with a relatively high extinction of up to $\simeq 2$ mag in the V band (even if these values are only reached in $\simeq 25$ per cent of the known GCs in Harris 1996); while not as extreme as the bulge line of sight, this direction provides still severe crowding levels – on the Galactic plane – coupled with significant reddening.

4.3 Simulated *Gaia* measurements

Each of the two clusters (see Section 4.1) was projected at three different distances of 5, 10 and 15 kpc and combined with each of the three backgrounds, to produce the 18 clusters in Table 2. A typical systemic RV of 100 km s^{-1} was assigned to each cluster (broadly compatible with the values listed in the Harris 1996, catalogue, in its most recent version), while a proper motion of -5 mas yr^{-1} in both the RA and Dec was assigned to all clusters (broadly compatible with the values measured by, e.g. Dinescu et al. 1999). Distances were also converted into parallaxes.

Integrated *Gaia* magnitudes G, G_{BP} and G_{RP} (see also Section 2 and Fig. 1) were obtained for each star using the formulae provided by Jordi et al. (2010, using their coefficients from Table 3), starting from the $B-V$ colour. For extinction, we adopted the pessimistic hypothesis that the cluster reddening was equal to the corresponding background field's highest value (i.e. as if the cluster was entirely behind the field population). While this assumption is not completely realistic, it gave us the possibility of exploring higher reddening conditions, at least for the disc projections. This yielded an A_{V} of 0.062 mag for the halo projections, 0.080 mag for the bulge projections and of 2.149 mag for the disc projections.

Table 3. Column-by-column description of the final simulated stars that will only be available in the electronic edition of the journal, and at CDS.

Content	Column	Units	Description
Cluster	(1)		Cluster number
Star	(2)		Star ID
RA′	(3)	(deg)	Position along the RA direction
Dec′	(4)	(deg)	Position along the Dec direction
δcoord	(5)	(deg)	Error on RA′ and Dec′
$\mu_{RA'}$	(6)	(mas yr^{-1})	RA′ proper motion
$\mu_{Dec}{'}$	(7)	(mas yr^{-1})	Dec′ proper motion
$\delta\mu$	(8)	(mas yr^{-1})	Error on proper motion
ϖ	(9)	(mas)	Parallax
$\delta\varpi$	(10)	(mas)	Parallax error
G	(11)	(mag)	G-band integrated magnitude
δG	(12)	(mag)	G magnitude error
G_{BP}	(13)	(mag)	G_{BP} integrated magnitude
δG_{BP}	(14)	(mag)	G_{BP} magnitude error
G_{RP}	(15)	(mag)	G_{RP} integrated magnitude
δG_{RP}	(16)	(mag)	G_{RP} magnitude error
Membership	(17)		True membership

Note. The pseudo-coordinates RA′ and Dec′ are just distances from the centre in deg, not true sky coordinates. The true membership, in the case of classic blends, relates to the brightest star of the blend. It is 1 for cluster members and 0 for field stars.
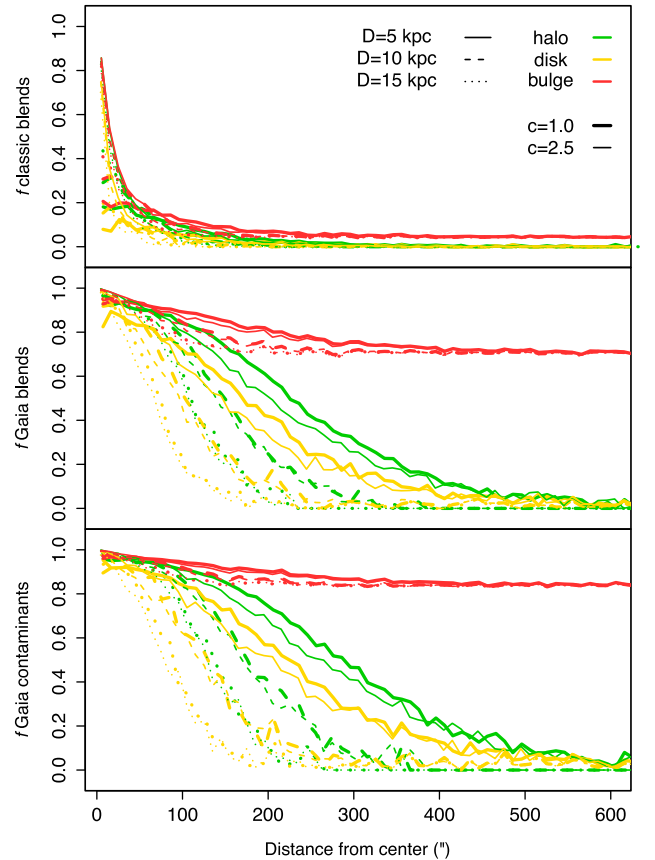
4.4 Crowding evaluation

For each simulated star in each GC, we counted all neighbours (with flux above 0.1 per cent of the star) within a specified distance, depending on the considered instrument and on the types of blends (Section 3). We adopted an exhaustive algorithm for neighbours search.[15]

The relative number of each type of neighbours (classic blends, *Gaia* blends, contaminants) for the 18 simulated clusters is shown in Fig. 8 as a function of distance from the GC centre. As can be seen, the parameter that dominates the fraction of classic blends is the GC concentration: core-collapsed clusters have more than twice the number of classically blended stars in their central parts compared to normal GCs. The vast majority of classic blends are in the GC central regions, and are blends of GC members with other GC members. Distance and reddening have a curious effect: because GCs become fainter with increasing distance and reddening, their luminosity function crosses the detection limit of *Gaia* where it is less populous. As a consequence, not only the number of stars detected by *Gaia* decreases, but also the probability of blending, and so the blends and contaminant fractions. On the other hand, the effect of field contaminants is to increase the fraction of *Gaia* blends and contaminants at all distances from the centre. Extreme cases are the bulge background GCs, where the vast majority of stars are blended and/or contaminated to some degree at all radii, mostly by field stars.

We listed in Table 2 some key quantities resulting from the crowding evaluation. As can be seen, the number of stars that are clean

---

[15] In other words, we looped over the list of (relevant) stars and computed distances with all other (relevant) stars, one object at a time. This was necessary because smarter neighbour searches pre-compute a distance matrix to increase computation speed, and therefore tend to saturate computer memory for data sets containing more than 10^5 objects (Hendra Gunadi 2011). Our bulge simulated GCs contain a few million stars, and several tens of millions of relevant pairs.

Figure 8. Results of the crowding evaluation on simulated GCs. Each panel displays the relative fraction of classic blends, *Gaia* blends and contaminants as a function of distance from the GC centre. Only stars that are blended or contaminated by at least 0.01 mag in total (i.e. $\simeq$1 per cent of their flux) are shown in the figure. Only classic blends have a significant effect on the astrometric performances, while BP/RP and RVS are significantly affected also by *Gaia* blends and contaminants.

(i.e. contaminated by less than 1 mmag) can be substantial when the background is not extreme. The vast majority of *Gaia* blends and contaminants will be known, as a large fraction of the classic blends (see Section 2.1.1). Therefore, it will always be possible to select a reliable sample of clean stars from *Gaia* data.

Additionally, we report here that already in the first *Gaia* release, which does not contain stars in truncated windows or stars with low-quality measurements (Gaia Collaboration 2016b), more than 200 000 stars were actually detected in the ω Cen field. This compares well with our #1 cluster, which is reasonable considering the higher mass of ω Cen, and gives support to the figures discussed above and reported in Table 2.

4.5 Simulated *Gaia* errors

To compute the *Gaia* errors, we combined the post-launch *Gaia* science performances (Gaia Collaboration 2016a) with our crowding error estimates. For the magnitudes we combined the two errors in quadrature, because they are fully independent. For the astrometric and spectroscopic measurements, the crowding errors are not fully independent from the *Gaia* science performances, because they both depend on the star magnitude. Therefore, we conservatively summed the errors in modulus.

4.5.1 Crowding errors

We used the modelling described in Section 3, which provided a relative error on the flux of each star, caused by the various type of blends and contaminants affecting it. These modelled errors represent well the crowding errors for G, G_{BP} and G_{RP}, i.e. on the photometry.

To evaluate the crowding errors on astrometry, we considered two components: the error on centroiding and a chromatic shift. For the centroiding errors, only classic blends were considered, because only stars closer than the PSF are expected to have a significant impact on the final centroid measurement of a star. We expect that the PSF of a star will be perturbed by the residual flux left by the close companions after the deblending procedure, and these residuals will depend on the contaminating flux and distance of the blending stars, as modelled in Section 3. We therefore computed the percentual flux in the residuals as an average of the blended star and the blending ones, weighted on distance and flux of the blending stars. We then assumed that the percentual centroiding error caused by blending was equal to this residual contaminating flux, a pessimistic assumption. The resulting centroiding errors caused by crowding are typically of the order of $\sim$10 µas yr^{-1} (with maximum values of $\sim$100), but they affect a relatively low number of stars in each GC (see Table 2).

For the chromaticity correction, we know that chromatic effects for *Gaia* are relevant, because of its high accuracy, and they are corrected using the BP/RP information. If an error is made on that colour determination because of blends, the error is transported into the astrometric measurements as well. It was estimated that the shift on the single *Gaia* measurement could amount to 500–800 µas, depending on the spectral type and on the position along the focal plane. By averaging out transits and by correcting the effect of spectral type with G_{BP}–G_{RP}, the residual end-of-mission errors would amount to 0.4–1.4 µas (Jordi et al. 2006)[16] in most of the well-behaved stars. However, for objects with non-stellar or peculiar colours, such as a quasar or a (multiple) stellar blend, the residual error could be still roughly 30 µas, as computed from the typical residual centroid shift difference between a B and an M star, after chromaticity correction (Jordi et al. 2006). We thus approximated linearly[17] the additional chromatic error as 0.002 µas for each K of temperature difference between each blended stars pair (both classic and *Gaia* blends), multiplied by the relative contaminating flux. The typical residuals from chromatic errors caused by crowding are of a few µas, but can be substantially higher for companions that are very bright or have a very different colour (up to $\simeq$30–50 µas in our simulations).

For RV error computations, the first consideration is that every time a star is contaminated by another star with a net RV difference above $\simeq$30 km s^{-1} (roughly the *Gaia* resolution element FWHM), there is a chance of separating the two RVs, depending on the relative flux contamination. The percentage of flux contamination (obtained as in Section 3) was used to degrade the signal of the contaminated (or blended) star. We thus recomputed the magnitude of each blended or contaminated star, taking into account the

residual errors after deblending or decontamination. We similarly recomputed the colours taking into account the residual colour errors. The recomputed colours and magnitudes were fed into the RV error equation (Gaia Collaboration 2016a), to derive the error on RV implied by the magnitude and colour deblending errors. The second consideration is that an artificial RV shift of roughly 30 km s^{-1} can also be obtained if two blended stars are offset, in the AL direction, by at least 4 AL pixels (or 0.235 arcsec), therefore we treated these stars as in the above case. We finally did not attempt to simulate any RV measurement for stars closer than the *Gaia* PSF (i.e. one AC pixel or 0.177 arcsec) as explained previously. Moreover, we did not compute RVs or RV errors for stars fainter than $G = 16$ mag.

5 RESULTS

We illustrate in the following sections the type of data quality we expect from *Gaia* at the end of the mission, based on our simulations. As mentioned already, given all the conservative assumptions and the use of preliminary deblending pipelines, the presented results have to be considered pessimistic, in the sense that the pipelines will be more sophisticated in a few years from now.

We will show in all figures three simulated GCs: an *easy case* with $D = 5$ kpc, $c = 1.0$ and a halo background (cluster #1, plotted in green in all figures); an *intermediate case* with 10 kpc, $c = 1.0$, and a disc background, with a relatively high reddening for GCs (cluster #5, plotted in yellow); and a *difficult case* with $D = 15$ kpc, $c = 2.5$, and a bulge background, which is an extreme condition for *Gaia* (cluster #18, plotted in red).
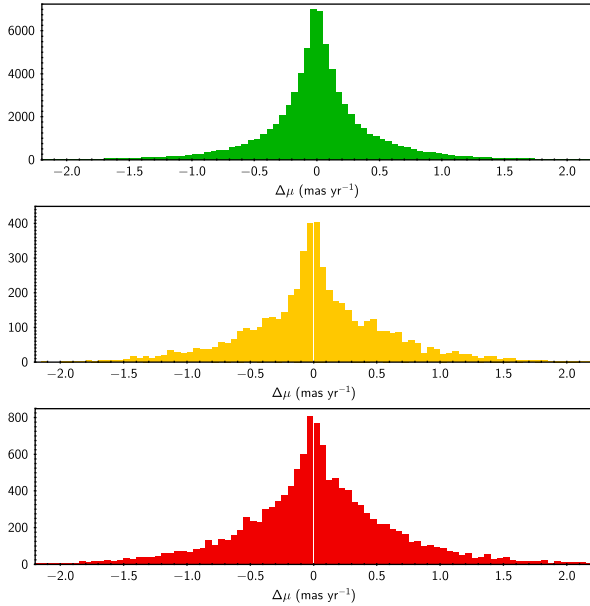
5.1 Proper motions

Because proper motions are determined with AF, the impact of crowding is less severe than on BP/RP spectrophotometry, or on RVS spectra. Fig. 9 shows the histogram of the differences between the final proper motion – including all error sources – and the initial error-free simulated one, for the known cluster members. The median systemic proper motion can be recovered with a bias of 5–10 µas yr^{-1}, i.e. with a systematic error of roughly 0.1–0.2 per cent. The intrinsic spread of the simulated GCs is of the order of 100 µas yr^{-1}, depending on the GC. The observed spread is around 400–500 µas yr^{-1}, if one includes all the simulated stars down to the magnitude limit. It is almost entirely explained with the nominal post-launch performances applied on top of the intrinsic spread, especially when including faint stars. In fact (see Section 4.5.1) the crowding errors *on the affected stars* are in the worst cases a few 100 µas yr^{-1} for the centroiding determination, and $\simeq$30 µas yr^{-1} for chromaticity errors caused by $G_{BP/RP}$ crowding errors.

Concerning individual stars, Fig. 10 shows the behaviour of the final simulated errors as a function of G magnitude. It can be useful to compare these simulations with the first results from the HST PROMO project for M15 (Hubble Space Telescope PROper MOtion project; Bellini et al. 2014). Their typical error around the $G = 15$ mag is 5–10 times higher than the error expected from *Gaia*, about 0.1 mas yr^{-1}, but at $G = 21$ mag they are about half the *Gaia* error, at 0.5 mas yr^{-1}. Moreover, *HST* proper motions can reach several magnitudes below the *Gaia* limit. On the other hand, the advantage of *Gaia*'s proper motions is that they cover a larger area around each GC – actually, the whole sky – and that they are *absolute* proper motions.

We show in Fig. 11 the typical vector diagrams of all simulated stars, including faint stars and background contaminants. The

---

[16] These estimates were computed using the *Gaia* filter system, now abandoned, but there are no other estimates available of the *Gaia* residual chromatic displacement in the literature at the moment.

[17] The entity of the chromatic correction errors caused by crowding is small for the simulated GCs (a few µas or µas yr^{-1}) compared to the *Gaia* science performances (see also Fig. 10), and therefore a linear approximation was considered adequate.
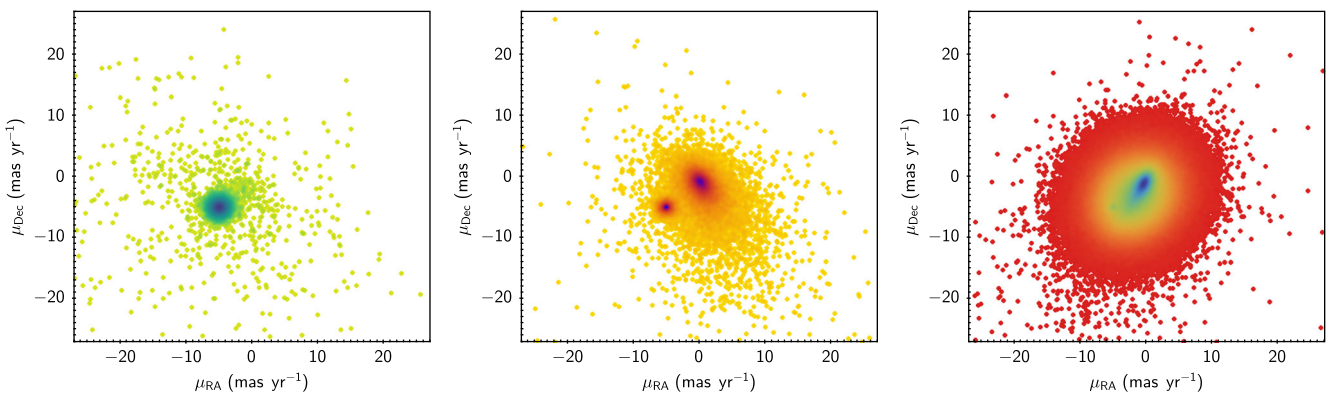
Figure 9. Histograms of differences between the final and error-free simulated proper motions of the easy (green histogram), intermediate (yellow histogram) and difficult cases (red histogram). Only cluster members are shown. The resulting absolute displacements in the systemic proper motion determination is of about 1–10 μas yr^{-1}, corresponding to errors of <0.1 per cent. We note that the intrinsic dispersion is of the order of 100 μas yr^{-1}, and the final, simulated one is 300–600 μas yr^{-1}, when including all stars down to $G \simeq 20.7$ mag.
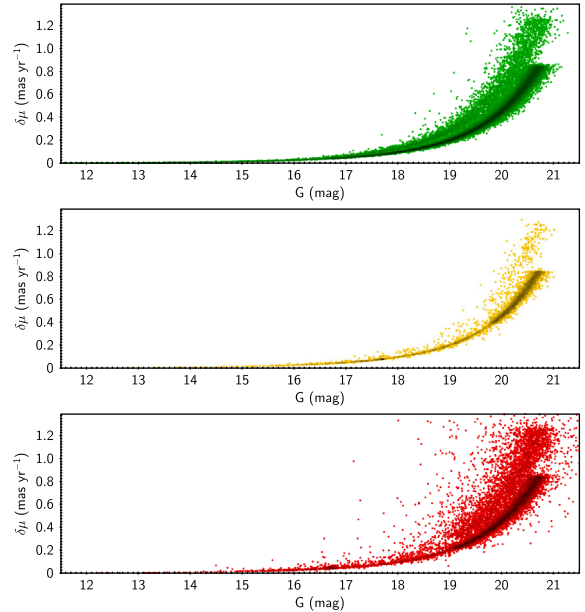
clusters are always easily separated from the field population, except in the case of the extreme bulge background. In the following sections, we will select the probable members with a *loose* criterium, i.e. stars within 1 mas yr^{-1} from the systemic GC motion, and with a *strict* criterium, i.e. within 0.3 mas yr^{-1} from the systemic GC motion.

5.1.1 Measurement of derived quantities

To assess the derived quantities that will be measurable from *Gaia* data, we performed a basic test on the easy case GC. We excluded all stars that were clearly unrelated to the GC with a very loose proper motion selection (± 3 mas yr^{-1}) and all the classic blends. We then converted proper motions in the RA and Dec directions
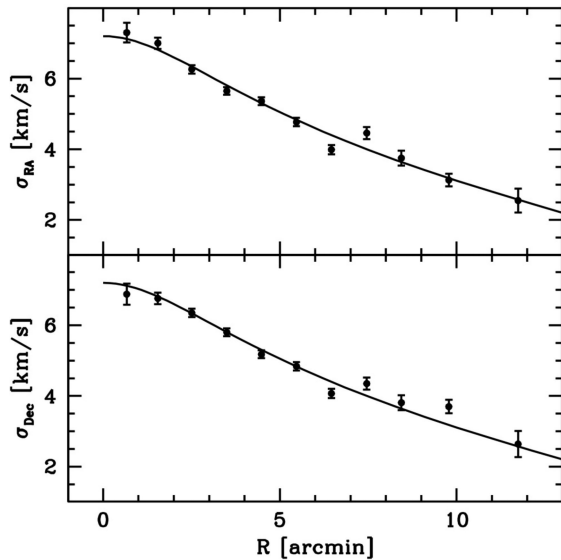

Figure 10. Final simulated proper motion errors, including the effect of crowding for the easy (green points), intermediate (yellow points) and difficult cases (red points), as a function of final simulated G magnitude. Only cluster members are shown.

into velocities, using the GC distance and propagating its error (see Section 5.2). We then estimated the RV spreads σ_{RA} and σ_{Dec} as a function of distance from the GC centre with their errors. We used the maximum likelihood estimation (MLE) method with the likelihood formulation described by Pryor & Meylan (1993), Walker et al. (2006) and Martin et al. (2007), which takes into account the errors on measurements as well. The actual errors on the RV dispersions in each radial bin are of about 0.4–1.4 km s^{-1}. The result is displayed in Fig. 12, showing that *Gaia* will be able to determine the radial profile of the RV dispersion of nearby GCs with errors of about 1 km s^{-1} in the nearest GCs.

More in general, we can say that:

(i) Proper motions obtained by *Gaia* in GCs will allow the study of dynamical relaxation in the 5–10 closest GCs (see also Section 5.3 and Fig. 14). This is because at least a few magnitudes below the GC turn-off point are required to adequately sample a range of stellar masses. Fig. 14 clearly shows that this is possible only for clusters

Figure 11. Proper motion diagrams for all the stars, cluster and background members, in the easy (green points), intermediate (yellow points) and difficult cases (red points). The colour scale refers to the density of points, with darker toner referring to higher densities. The cluster lies at $(-5, -5)$ in all diagrams, and it is always easily recognized, but it is overwhelmed by field stars in the last case.

Figure 12. RV dispersion profile in RA and Dec for the easy case cluster.

at $\simeq 5$ kpc or less, because of the *Gaia* detection limit. Therefore, these studies will have to rely on deeper proper motion data sets for more distant GCs.[18]

(ii) Two past studies dealt with the determination of masses in GCs with *Gaia* data (An, Evans & Deason 2012; Sollima et al. 2015) yielding somewhat conflicting results. The main problem is to break the mass-anisotropy degeneracy, with the anisotropy signal being stronger outside the central regions where relaxation has the highest effect. Therefore, blends by cluster members are irrelevant there, as discussed in Section 4.4 and shown in Fig. 8. And even in the case of heavy background contamination, proper motions will be only mildly affected (Fig. 10). The assumption by Sollima et al. (2015) that one can only use stars contaminated by less than 10 per cent of the flux by objects more distant than 3.54 arcsec, is far too pessimistic. The simulations by An et al. (2012), prove that 10 per cent mass estimates can be provided for GCs if one can count on at least 100 tracers (we can use red giants) with proper motion errors <100 µas. As shown in Table 2 and Fig. 10, the number of stars per GC with these errors will be more like a few 10^3–10^4, except maybe for the most extreme cases of bulge clusters. Moreover, our test with the easy GC above shows that RV spreads can be measured as a function of distance from the centre with 1 km s^{-1} errors at 5 kpc. Therefore, as concluded by An et al. (2012), it will be possible to determine GC masses with an error of 10 per cent or less at least up to 15 kpc. This requires ground-based RVs to complement *Gaia* proper motions.[19]

(iii) Gaia will be able to provide the necessary quantities for computing accurate GC orbits within the Galaxy, because, as we saw, it will provide high-quality systemic proper motions for each

GC, with a bias of a few µas yr^{-1} and errors of the order of 1 per cent. Distances will be obtained with similar errors, as discussed below (Section 5.2).

(iv) Once the orbits are obtained they could in turn be used to look for extra tidal stars and tidal tails. Even if the $G < 20.7$ mag limit reduces the density of targets that will be actually measured by *Gaia* around GCs, the proper motion signal of escaped GC stars should be very sharp, and in most cases significantly different – within the uncertainties – from that of the surrounding field population (see also Fig. 11).
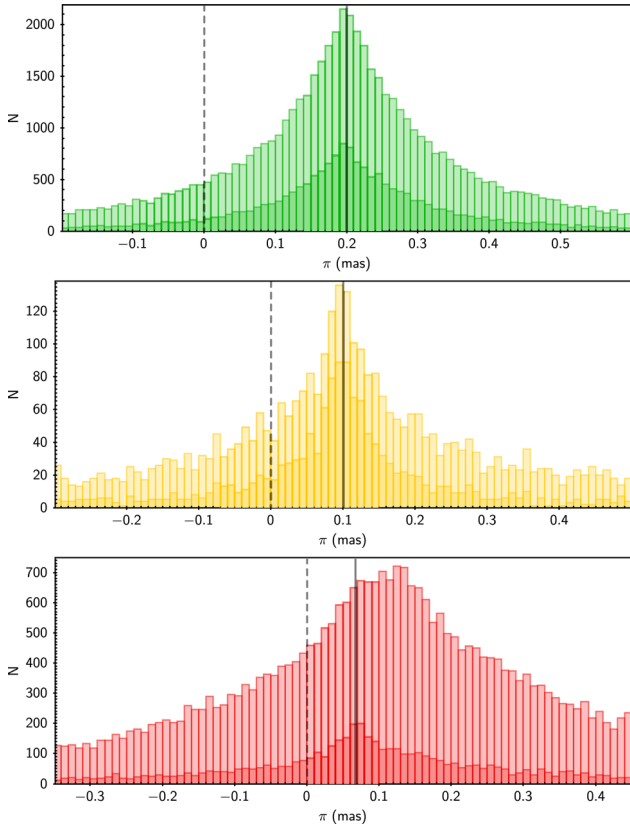
(v) *Gaia* could be able to help in the open and hotly debated problem of multiple populations (Kraft 1994; Gratton, Sneden & Carretta 2004), in particular by revealing kinematical differences among different GC sub-populations, if they are present (Hénault-Brunet et al. 2015). For example, Bellazzini et al. (2012) reported the possible detection of a different rotation pattern between the Na-rich and Na-poor stars in some of the GCs in their sample, with rotation amplitude differences not larger than $\simeq 5$ km s^{-1}. Depending on the distance and the inclination of the rotation axis, this would correspond, in terms of proper motions, to a difference in rotation of the order of 1 mas yr^{-1}, which would be detectable for those GCs having at least 100 stars with measurement errors of a few 10 µas.

5.2 Parallaxes

The major problem in deriving distances from parallaxes, especially when the error is comparable to the measurement, is that the errors on distances are not symmetric: by simply inverting the parallax one could obtain a very wrong distance estimate (Bailer-Jones 2015). Statistically speaking, it is also possible to obtain negative parallaxes, as illustrated in Fig. 13, which would result in meaningless distance estimates if not treated properly.

When one is interested in the systemic distance of a GC, however, negative parallaxes are useful to assess the uncertainty on the measurements and their distribution. Fig. 13 shows the distribution of parallaxes for probable members, as defined in Section 5.1. As can be seen, not only the average parallax of the clusters is very well recovered, but also its uncertainty, provided that one makes use also of the negative parallaxes. The exception is the case of the difficult cluster, which has a background contamination that overwhelms the signal from the cluster members. As can be seen, the recovered parallax is strongly biased by the background contaminants. A more strict members selection apparently produces better results (but see below). However, the resulting distribution of strict members is still asymmetric, because of the blends between cluster and field stars.

This type of problem is not specific of *Gaia* data, of course, but it is extremely important to employ a reliable membership selection and robust statistical modelling of the parallax distribution, which can be skewed and is heteroscedastic. We employed an MLE analysis of the 18 simulated GCs using the strict and loose membership criteria described above. We used the likelihood estimator described by Pryor & Meylan (1993), Walker et al. (2006) and Martin et al. (2007), which takes into account the highly variable errors, and we computed the most probable parallax ϖ and its error $\delta\varpi$. The result is displayed in Table 4. We first note that the depth of a GC, as measured with parallaxes, can correspond at most to a few µas for the nearest GCs that have large radii, even if one considers the tidal radius, and in the majority of cases is well below 1 µas. Thus the observed spread is caused almost entirely by measurement errors. The bias itself, i.e. the difference between the true input parallax

---

[18] Deeper measurements could be obtained if the mission lifetime is extended beyond its nominal 5-yr duration. The SEA pipelines also have the potential of recovering faint stars. Finally, the use of the 2D images obtained for some crowded fields will help by directly recovering some faint stars and by improving the deblending pipelines, thus recovering more faint stars also in other regions.

[19] For the closest GCs, *Gaia* will provide some good RVs as well, see also Section 5.4, for more details.

Figure 13. Histograms of the parallaxes for the easy (top panel), intermediate (middle panel) and difficult (lower panel) clusters. The vertical dotted line in all panels marks the zero parallax limit, while the solid line marks the true parallax of each simulated GC. Lightly shaded histograms show the member stars selected with the loose criterium and heavily shaded ones with the strict criterium (see Section 5.1).

Table 4. Systemic parallax for the simulated clusters, based on members selected with the strict and loose criteria (see text for more details). The columns contain: (1) the cluster number; (2) concentration parameter; (3) projected cluster distance and (4) parallax; (5) background type; (6) systemic parallax and error for members selected with the strict criterium and (7) with the loose criterium.

Cluster	c	D_0 (kpc)	ϖ_0 (μas)	Field	ϖ_{strict} (μas)	ϖ_{loose} (μas)
# 1	1.0	5	200.0	Halo	200.2 ± 2.6	200.2 ± 0.6
# 2	1.0	10	100.0	Halo	101.6 ± 2.1	99.3 ± 0.8
# 3	1.0	15	66.7	Halo	69.2 ± 2.6	69.1 ± 1.0
# 4	1.0	5	200.0	Disc	203.9 ± 6.1	197.4 ± 1.3
# 5	1.0	10	100.0	Disc	95.6 ± 4.4	98.5 ± 1.5
# 6	1.0	15	66.7	Disc	74.0 ± 5.6	65.8 ± 1.9
# 7	1.0	5	200.0	Bulge	206.8 ± 2.3	200.8 ± 0.6
# 8	1.0	10	100.0	Bulge	100.1 ± 1.9	99.1 ± 0.6
# 9	1.0	15	66.7	Bulge	63.9 ± 2.3	67.9 ± 0.7
# 10	2.5	5	200.0	Halo	197.5 ± 0.7	198.4 ± 0.4
# 11	2.5	10	100.0	Halo	101.4 ± 1.3	101.2 ± 0.6
# 12	2.5	15	66.7	Halo	62.2 ± 1.5	66.4 ± 0.9
# 13	2.5	5	200.0	Disc	200.0 ± 1.6	200.2 ± 0.8
# 14	2.5	10	100.0	Disc	100.0 ± 3.1	102.8 ± 1.3
# 15	2.5	15	66.7	Disc	74.3 ± 3.2	70.5 ± 1.8
# 16	2.5	5	200.0	Bulge	199.3 ± 0.7	198.6 ± 0.4
# 17	2.5	10	100.0	Bulge	101.6 ± 1.3	99.5 ± 0.5
# 18	2.5	15	66.7	Bulge	65.8 ± 1.4	67.0 ± 0.7

and the recovered one, is always 1 per cent or smaller, even for the difficult case GC. The formal error on the recovered ϖ is of the same order. We also note that choosing a more restrictive membership selection can often increase the formal errors without resulting in a better ϖ determination. On the contrary, the bias is slightly increased when applying a more restrictive membership selection (see also Bailer-Jones 2015).

The scientific implications of ≃1 per cent distances for most of the GCs in the Galaxy are far reaching. They directly help in the determination and modelling of GC orbits, which can then be used for dynamical studies of the MW, of the GC themselves, and of the interactions between the two. For example, they would help simulations that use the GC orbits and tidal tails and streams to constrain the Galactic potential (Peñarrubia, Koposov & Walker 2012; Price-Whelan et al. 2014), or they can help discerning the origin of the GC themselves through dynamical modelling. But the area in which significant breakthrough is expected lies in the determinations of stellar ages (Gratton et al. 1997) and masses (Feuillet et al. 2016). Distance has in fact a similar effect as age when using high-quality CMDs (from *HST* or ground-based observations) to estimate the *absolute ages* of GCs. By reducing the distance determination errors by more than a factor of 10, we can expect a significant improvement on the age determinations, obtaining absolute ages with errors below 10 per cent. On the other hand, ≃1 per cent distances can help in constraining the stellar masses and more importantly, the surface gravities. When trying to determine *relative ages* in GCs with multiple stellar populations, one needs to disentangle the effects of chemical composition – mainly helium and C+N+O abundance – from age effects. A very accurate surface gravity determination would remove one of the major sources of uncertainty in the determination of stellar chemistry from spectroscopy.

5.3 Photometry

The *Gaia* colour–magnitude diagrams (CMDs) of the three example clusters are shown in Fig. 14. The top panels show all the simulated stars, including the background, while the bottom panels show only the probable members, selected with the loose criterium described in the previous section. As can be seen, background contamination is the first obvious cause of crowding errors for *Gaia* photometry. A large reddening (like in the case of the disc cluster) or a distance larger than 10 kpc also impact the quality of the CMD, because the photometric errors, especially those on the G_{BP}–G_{RP} colour, increase quite rapidly with magnitude.

It will therefore not be possible to reach the nominal photometric errors promised by *Gaia* in those clusters that lie on a bulge or disc background. This is mainly caused by the extended shape of the BP and RP dispersed images, while the G magnitudes will not suffer significantly from crowding. However, for clusters that are relatively free from background contamination, the BP/RP photometry of stars brighter than $G \simeq 15$ mag will have an extremely good quality, comparable to *HST* photometry. Fainter stars down to $G \simeq 18$–19 mag will still have a BP/RP quality that is comparable with the best ground-based catalogues.

While *HST* photometry will certainly be preferable for some applications, *Gaia* photometry will have a few advantages: (1) the field of view of *Gaia* is not limited by any field size: it covers the whole sky; (2) each star that has *Gaia* astrometry from AF, also has BP/RP spectra from which rough stellar parameters and a reddening estimate can be obtained (Gaia Collaboration 2016a); (3) brighter stars, generally red giants in the case of GCs, will also
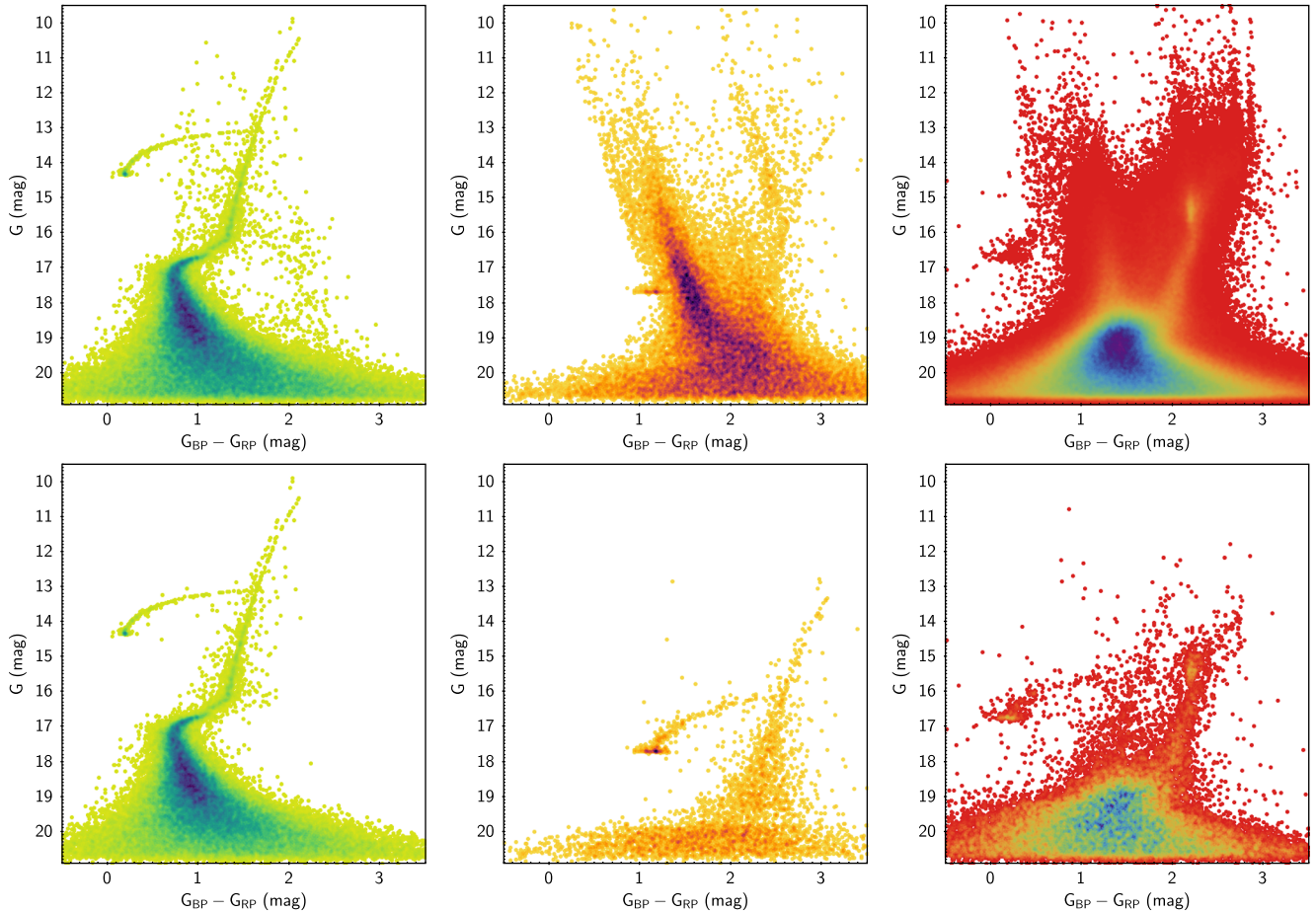
Figure 14. The simulated *Gaia* photometry for the three example GCs. Top panels show all the simulated stars, regardless of membership. Bottom panels show only the loosely selected probable members (see text for more details). The left-hand panels refer to the easy case, the centre ones to the intermediate case and the right ones to the difficult case. The colour scale refers to the density of points, with darker toner referring to higher densities.

have RVs and more accurate estimates of parameters and reddening from RVS spectra[20] (Kordopatis et al. 2012) and (4) the absolute photometric calibration of *Gaia* will be based on one the largest, most homogeneous, and most accurate set of spectrophotometric standard stars to date (Pancino et al. 2012; Altavilla et al. 2015; Marinoni et al. 2016), that will grant an accuracy of ≃1–3 per cent with respect to Vega (Bohlin & Gilliland 2004).

5.4 Radial velocities

Stars brighter than $G \simeq 17$ mag will have RVs measurements. *Gaia* has already produced billions of RVS spectra and by the end of the mission, each star will be observed on average 40 times. This can be compared with the extremely successful RAVE survey (Radial VElocity Experiment; Kordopatis et al. 2013), which measured RVs for half a million stars with $V < 12$ mag. The *Gaia* end-of-mission errors will vary with the star's colour and will be of the order of $1 \, \text{km} \, \text{s}^{-1}$ for the bright red stars ($G < 12.5$ mag and cooler than F types) and will be about 15–$20 \, \text{km} \, \text{s}^{-1}$ or more for fainter and
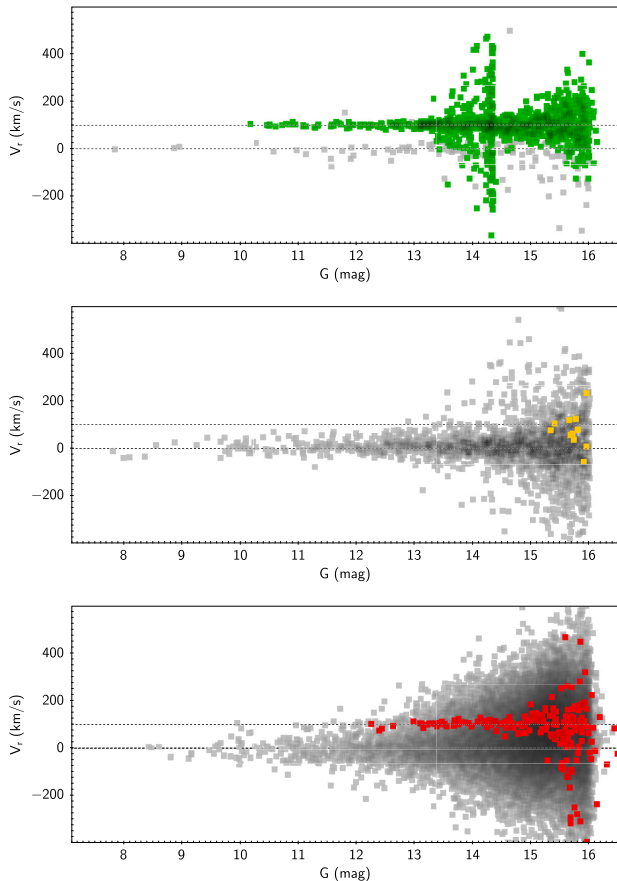
bluer stars. Crowding will affect RVS more than any of the other instruments on board. Even if the magnitude limit is brighter, the AL size of the spectra is more than an arcminute on the sky (see Table 1).

Fig. 15 shows the simulated RV measurements, as a function of the G magnitude, for the three example cases. Given the limitations of our simulations, we immediately note that only a handful of reliable members in the intermediate case have meaningful RV determinations, because of the combined effect of high reddening – for a GC – and background contamination. We also note the large scatter in RV for the faintest stars in the difficult case, where background contamination takes its toll. However, for the easy case, we notice that a sample of more than 100 stars with magnitudes above ≃13–14 mag is available, with errors around 1 or few km s^{-1}. This will happen for the closest 10–20 GCs. The stars with large errors between 13.5 and 14.5 mag are hotter HB stars. To conclude, we note that a mission extension would increase the quality of the RVS spectra.

5.5 The central arcminute

As discussed in Section 2.2, it is not feasible to simulate the degree of completeness of *Gaia* data, because it varies across the sky, based on the number of different passages and on their respective orientation.

[20] Accurate reddening estimates can also be obtained from diffuse interstellar bands, that are included in the *Gaia* RVS wavelength range (see, for example Puspitarini et al. 2015, and references therein).
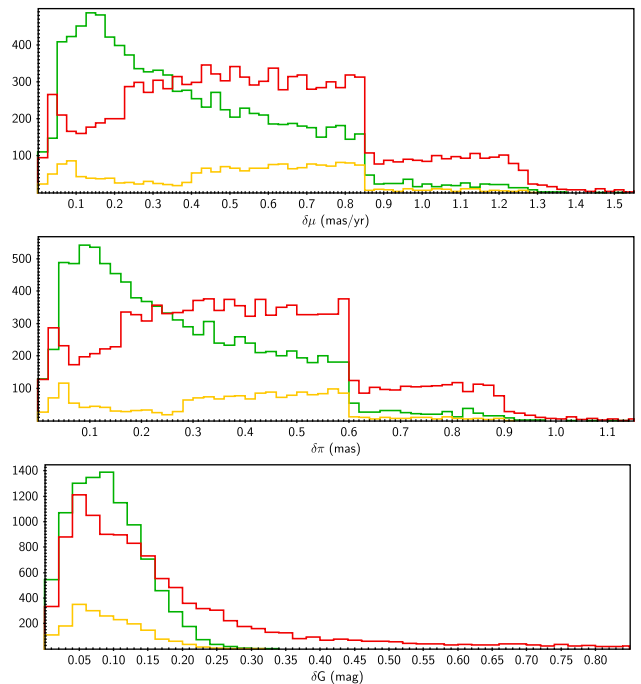
Figure 16. End-of-mission error distribution for all member stars (defined as in Fig. 15) down to $G = 20.7$ mag, within the central arcminute of the simulated GCs. The top panel shows proper motion errors, the middle one parallax errors and the bottom ones G magnitude errors. The easy cluster is represented in green in all panels, the intermediate one in yellow and the difficult one in red.

Figure 15. RV as a function of magnitude for the easy (top panel), medium (middle panel) and difficult (bottom panel) cases. The entire samples of available RV measurements are plotted in grey. The dotted lines mark zero and the true systemic velocity of the simulated clusters, $100 \, \mathrm{km \, s^{-1}}$. Only true cluster members are coloured in green, yellow and red, respectively.

As discussed in that section, nearby and relatively sparse GCs like ω Cen should be 100 per cent complete down to $V \simeq 16$ mag, even in the very core. This might appear surprising, but it is a beneficial byproduct of the relatively shallow *Gaia* magnitude limit.

However, still the question remains: how far into the GC core can we obtain reliable measurements, at least for the stars that we will be able to measure? Fig. 16 shows the end-of-mission error distributions for all member stars, down to $G = 20.7$ mag, for the central arcminute of the simulated clusters. As can be seen, astrometry is not too badly affected by crowding: the maximum errors are of 1 mas yr^{-1} for proper motions and 0.7 mas for parallaxes (to compare with Fig. 10). The majority of stars have performances of the order of a few hundred μas yr^{-1} or μas, and this including also the faintest stars. If this appears surprising, we recall that what mostly governs the end-of-mission astrometric errors caused by crowding in *Gaia* is the PSF size, which is comparable to that of *HST*.

The situation is different for BP/RP photometry or RVS, because even if the PSF in the AC direction is still small, and thus allows to detect blends quite efficiently, the AL size of the window is larger, and aligned with the dispersion axis of the spectra. The performances in the central arcminute are in fact significantly worse for these instruments than for the AF and the G-band magnitude in the case of crowded fields.

6 SUMMARY AND CONCLUSIONS

We used all the available information on the presently available *Gaia* deblending pipelines, along with their results on simulated data, to model the behaviour of *Gaia* in crowded areas. We computed additional crowding errors that were combined with the post-launch science performances of *Gaia* and applied to a set of simulated GCs with different concentration ($c = 1.0$ and 2.5), distance (5, 10 and 15 kpc), and field population (halo, disc and bulge).

We showed that:

(i) *Gaia* will provide estimates of the parallax and systemic motion of GCs with unprecedented accuracies: $\simeq 1$ per cent and $\ll 1$ per cent, respectively, for all GCs as far as 15 kpc at least. Also, systemic RVs with errors of a few km s^{-1} will be obtained for the 10–20 closest GCs, although our RVS simulations are not as accurate as for the other *Gaia* instruments. This will allow for a very accurate modelling of GC orbits.

(ii) The astrometry, obtained through the AF together with G magnitudes, will be only marginally affected by crowding, having performances not too dissimilar from the nominal *Gaia* performances even for the most field-contaminated bulge GCs. This is an effect of the tiny *Gaia* PSF (0.17 arcsec) in AF. The G magnitudes will have mmag performances and space quality to $G \simeq 17$–18 mag.

(iii) The proper motions of individual stars within GCs have sufficient quality to obtain mass estimates with 10 per cent errors for GCs as far as 15 kpc at least, and to identify small variations of the properties (rotations, spreads) of a few km s^{-1} for GCs as far as 10 kpc.

(iv) The distances of GCs will be obtained with errors of $\simeq 1$ per cent, and for GCs heavily contaminated by field stars to a few per cent. The impact on the determinations of stellar masses and ages will be significant. It is expected that GC absolute ages with errors below 10 per cent will be obtained. Also, better estimates of surface gravities for GC stars with known distances will remove one of the major uncertainty sources from abundance determinations with high-resolution spectroscopy.

(v) While it is difficult to simulate the exact completeness level of *Gaia* in GCs, we have shown that the astrometric performances are still exceptional in the central arcminute of the simulated GCs: most of the stars have errors around a few 100 μas or μas yr^{-1}.

(vi) The BP/RP photometry and the RVS spectra, on the other hand, have larger AL sizes and therefore suffer more from crowding effects. The most important factor for these instruments is crowding by field stars, especially in the most extreme cases like the bulge field, which acts at all distances from the GC centre and combines with the crowding effects from GC stars in the central regions.

The imminent decision of whether to extend the *Gaia* mission lifetime will certainly have a beneficial impact on all the above measurements. However, the simulations presented here are already pessimistic and the pipelines are expected to evolve significantly in the next few years. Therefore, we conclude that *Gaia* measurements will revolutionize our knowledge of GCs.

ACKNOWLEDGEMENTS

REFERENCES

Allende Prieto C., 2008, Gaia Technical Note number GAIA-C6-SP-MSSL-CAP-003
Altavilla G., Botticella M. T., Cappellaro E., Turatto M., 2012, Ap&SS, 341, 163
Altavilla G. et al., 2015, Astron. Nachr., 336, 515
An J., Evans N. W., Deason A. J., 2012, MNRAS, 420, 2562
Babusiaux C., 2005, in Turon C., O'Flaherty K. S., Perryman M. A. C., eds, ESA SP-576: The Three-Dimensional Universe with Gaia. ESA, Noordwijk, p. 417
Bachchan R. K., Hobbs D., Lindegren L., 2016, A&A, 589, A71
Bailer-Jones C. A. L., 2015, PASP, 127, 994
Bellazzini M., Bragaglia A., Carretta E., Gratton R. G., Lucatello S., Catanzaro G., Leone F., 2012, A&A, 538, A18
Bellini A. et al., 2014, ApJ, 797, 115
Bohlin R. C., Gilliland R. L., 2004, AJ, 127, 3508
Brodie J. P., Strader J., 2006, ARA&A, 44, 193
de Bruijne J. H. J., Rygl K. L. J., Antoja T., 2014, EAS Publ. Ser. Vol. 67, Gaia Astrometric Science Performance – Post-Launch Predictions. EDP Sciences, Les Ullis, p. 23
de Bruijne J. H. J., Allen M., Azaz S., Krone-Martins A., Prod'homme T., Hestroffer D., 2015, A&A, 576, A74

Dinescu D. I., van Altena W. F., Girard T. M., López C. E., 1999, AJ, 117, 277
Ducourant C., Krone-Martins A., Galluccio L., Teixeira R., 2014, in Ballet J., Martins F., Bournaud F., Monier R., Reylé C., eds, Proc. Ann. French Soc. Astron. Astrophys., Gaia and the Extragalactic. p. 421
Eyer L. et al., 2014, in Walton N. A., Figueras F., Balaguer-Núñez L., Soubiran C., eds, EAS Publ. Ser. Vol. 67, The Milky Way Unravelled by Gaia: GREAT Science from the Gaia Data Releases. p. 75
Fabricius C. et al., 2016, A&A, 595, A3
Feuillet D. K., Bovy J., Holtzman J., Girardi L., MacDonald N., Majewski S. R., Nidever D. L., 2016, ApJ, 817, 40
Gaia Collaboration, 2016a, A&A, 595, A1
Gaia Collaboration, 2016b, A&A, 595, A2
Gratton R. G., Fusi Pecci F., Carretta E., Clementini G., Corsi C. E., Lattanzi M., 1997, ApJ, 491, 749
Gratton R., Sneden C., Carretta E., 2004, ARA&A, 42, 385
Harris W. E., 1996, AJ, 112, 1487
Harrison D. L., 2011, Exp. Astron., 31, 157
Hendra Gunadi A., 2011, Master thesis, Australian National University
Hénault-Brunet V., Gieles M., Agertz O., Read J. I., 2015, MNRAS, 450, 1164
Hurley J. R., Pols O. R., Tout C. A., 2000, MNRAS, 315, 543
Høg E. et al., 2000, A&A, 355, L27
Jordi C. et al., 2006, MNRAS, 367, 290
Jordi C. et al., 2010, A&A, 523, A48
King I. R., 1966, AJ, 71, 64
Kordopatis G., Recio-Blanco A., de Laverny P., Bijaoui A., Hill V., Gilmore G., Wyse R. F. G., Ordenovic C., 2012, EPJ Web Conf., 19, 09010
Kordopatis G. et al., 2013, AJ, 146, 134
Kraft R. P., 1994, PASP, 106, 553
Kroupa P., 2001, MNRAS, 322, 231
Küpper A. H. W., Maschberger T., Kroupa P., Baumgardt H., 2011, MNRAS, 417, 2300
Lindegren L. et al., 2016, A&A, 595, A4
Marinoni S. et al., 2016, MNRAS, 462, 3616
Martin N. F., Ibata R. A., Chapman S. C., Irwin M., Lewis G. F., 2007, MNRAS, 380, 281
Michalik D., Lindegren L., Hobbs D., 2015, A&A, 574, A115
Mignard F., 2005, in Seidelmann P. K., Monet A. K. B., eds, ASP Conf. Ser. Vol. 338, Astrometry in the Age of the Next Generation of Large Telescopes. Astron. Soc. Pac., San Francisco, p. 15
Mora A. et al., 2016, in MacEwen H. A., Fazio G. G., Lystrupeds M., Batalha N., Siegler N., Tong E. C., eds, Proc. SPIE Conf. Ser. Vol. 9904, Space Telescopes and Instrumentation 2016: Optical, Infrared, and Millimeter Wave. SPIE, Bellingham, p. 99042D
Pancino E. et al., 2012, MNRAS, 426, 1767
Pancino E., Bellazzini M., Marinoni S., 2013, Mem. Soc. Astron. Ital., 84, 83
Paust N. E. Q. et al., 2010, AJ, 139, 476
Peñarrubia J., Koposov S. E., Walker M. G., 2012, ApJ, 760, 2
Perryman M. A. C. et al., 1997, A&A, 323, 49
Perryman M. A. C. et al., 2001, A&A, 369, 339
Piersimoni A., De Luise F., Busso G., 2011, Gaia Technical Note number GAIA-C5-TN-OATE-AP-001
Pourbaix D., 2011, in Docobo J. A., Tamazian V. S., Balega Y. Y., eds, AIP Conf. Proc. Vol. 1346, International Workshop on Double and Multiple Stars: Dynamics, Physics, and Instrumentation. Am. Inst. Phys., New York, p. 122
Price-Whelan A. M., Hogg D. W., Johnston K. V., Hendel D., 2014, ApJ, 794, 4
Proft S., Wambsganss J., 2015, A&A, 574, A46
Pryor C., Meylan G., 1993, in Djorgovski S. G., Meylan G., eds, Proc. ASP Conf. Ser. Vol. 50, Structure and Dynamics of Globular Clusters. Astron. Soc. Pac., San Francisco, p. 357
Puspitarini L. et al., 2015, A&A, 573, A35
Robin A. C., Reylé C., Derrière S., Picaud S., 2003, A&A, 409, 523
Seabroke G. et al., 2016, in Bragaglia A., Arnaboldi M., Rejkuba M., Romano D., eds, Proc. IAU Symp. 317, The General Assembly of Galaxy

Halos: Structure, Origin and Evolution. Cambridge Univ. Press, Cambridge, p. 346

Sollima A., Baumgardt H., Zocchi A., Balbinot E., Gieles M., Hénault-Brunet V., Varri A. L., 2015, MNRAS, 451, 2185

Sollima A. et al., 2016, MNRAS, 462, 1937

Tanga P. et al., 2016, Planet. Space Sci., 123, 87

Taylor M. B., 2005, in Shopbell P., Britton M., Ebert R., eds, ASP Conf. Ser. Vol. 347, Astronomical Data Analysis Software and Systems XIV. Astron. Soc. Pac., San Francisco, p. 29

Walker M. G., Mateo M., Olszewski E. W., Bernstein R., Wang X., Woodroofe M., 2006, AJ, 131, 2114

Zwitter T., Kos J., 2015, Mem. Soc. Astron. Ital., 86, 541

SUPPORTING INFORMATION

Supplementary data are available at *MNRAS* online.

Table 3. Column-by-column description of the final simulated stars.

Please note: Oxford University Press is not responsible for the content or functionality of any supporting materials supplied by the authors. Any queries (other than missing material) should be directed to the corresponding author for the article.

APPENDIX A: LIST OF ACRONYMS

Table A1 lists all the acronyms used.

Table A1. List of acronyms used in this paper.

Acronym	Description
AC	ACross scan
AF	Astrometric field
AL	ALong scan
BP	Blue spectro-Photometer
CCD	Charge-coupled device
CDS	Centre de Données astronomiques de Strasbourg
CMD	Colour–magnitude diagram
CNES	Centre National d'Études Spatiales
DPAC	Data Processing and Analysis Consortium
ESA	European Space Agency
FWHM	Full width at half-maximum
GIBIS	Gaia Instrument and Basic Image Simulator
GC	Globular cluster
HB	Horizontal branch
HST	*Hubble Space Telescope*
IMF	Initial mass function

Table A1 – *continued*

Acronym	Description
LSF	Line spread function
MLE	Maximum likelihood estimator
MW	Milky Way
NSS	Non-single stars
PSF	Point spread function
RAVE	RAdial Velocity Experiment
RP	Red spectro-Photometer
RV	Radial velocity
RVS	Radial velocity spectrometer
SEA	Source Environment Analysis
SM	Sky Mapper
TDI	Time-delayed integration

This paper has been typeset from a TEX/LATEX file prepared by the author.